

Superfluid Band Theory for the Rod Phase in the Magnetized Inner Crust Matter: Entrainment, Spin-orbit Coupling, and Spin-triplet Pairing

Kenta Yoshimura and Kazuyuki Sekizawa

*Department of Physics, School of Science, Institute of Science Tokyo, Tokyo
152-8550, Japan*

.....

The inner crust of neutron stars hosts a rich variety of nuclear phenomena and provides a unique opportunity for exploring microscopic nuclear properties relevant to diverse astrophysical observations. In particular, magnetars, which possess extremely strong magnetic-field, have attracted increasing interest in connection with nuclear spin dynamics and unconventional pairing correlations. This work is dedicated to develop a comprehensive theoretical framework to describe structures and properties of two-dimensional crustal matter (i.e., rod phase) in the inner crust of neutron stars, incorporating band-structure effects, neutron spin-triplet pairing, and strong magnetic-fields on an equal footing. Nuclear interactions and correlations are treated within the framework of nuclear density functional theory combined with a local description of pairing correlations, known as the superfluid local density approximation. Within this framework, the definition of the anomalous density is generalized to include spin-triplet components, and a spin-triplet pairing energy density functional is consistently incorporated. The main results of this study can be summarized as follows. In the first place, magnetic-fields of the order of 10^{16} G are found to substantially enhance the neutron effective mass by a factor of approximately 1.5, indicating a significant modification of entrainment properties in strongly magnetized crustal matter. In the second place, while the overall behavior of pairing phase transitions is qualitatively similar to that observed in one-dimensional systems studied previously, the present two-dimensional calculations reveal a nontrivial role of the spin-orbit interaction in inducing spin-polarization under magnetic-fields. In the third place, concerning the spin-triplet superfluidity, the rank-0 component is shown to emerge as a consequence of magnetic-field-induced spin-polarization, irrespective of the presence of spin-triplet pairing interactions, whereas the rank-2 component appears only when the corresponding interaction channel is included. These findings provide new microscopic insights into superfluid and magnetic phenomena in the inner crust of neutron stars and offer a theoretical basis for future studies of magnetars and related astrophysical processes.

arXiv:2601.13636v2 [nucl-th] 4 Feb 2026

1 INTRODUCTION

Neutron stars are compact objects which serve as natural laboratories for probing the nuclear and hadronic properties through the verification with the astronomical observations [1, 2]. The inner crust region in a neutron star is composed of the Coulomb lattice of nuclei coexisting with free neutron gas [3–7], where neutron superfluidity plays an indispensable role [8–11]. Superfluid properties in the neutron-star crust are believed to have impacts on various astrophysical phenomena associated with neutron stars, such as pulsar glitches and neutron-star cooling [12–16]. However, their detailed behavior can be altered radically by effects of the crystalline structures of nuclei including nuclear pasta phases, making a comprehensive analysis extremely challenging. For example, band-theoretical calculations applied to the inner-crust matter have suggested that the *effective mass* of free neutrons may be enhanced by factors of several up to around ten due to crystalline-structure effects [17–20]. This phenomenon, referred to as the *entrainment* effect, continues to be a subject of intense controversy, which involves consistency with pulsar glitch interpretations [21–23]. Subsequently, calculations incorporating self-consistency and superfluidity have been performed [24–26], and a variety of methodologies have been proposed, including approaches in which the effective mass is extracted from the dynamical response through time evolutions [27, 28], as well as methods to determine the superfluid fraction from its static properties [29–32]. Within these researches regarding the neutron effective mass or superfluid fraction, it was often the case that only the 1S_0 component was taken into considerations. However, in the context of astronomical simulations, the impact of spin-triplet superfluidity, such as the 3P_2 component, has been actively investigated [15, 23, 33–49], and these studies are pushing their physical interpretation to the next stage. Although spin-triplet components are generally expected to emerge only in the neutron-star core region [10, 50], recent studies have begun to suggest their existence in the crustal matter or even in finite nuclei. For example, in Ref. [51], it has been pointed out that, owing to the contribution of the spin-orbit interaction, 3P_1 superfluid components emerge in several open-shell nuclei. Another example is Ref. [52] where they revealed that spin-polarized neutron matter may produce the 3P_0 pairing component. There is a kind of neutron stars known as *magnetars* [53–55], which possess surface magnetic-fields exceeding 10^{14} G and possibly reaching up to 10^{17} or 10^{18} G [56–60]. In such matter with enormous magnetic-fields, the nuclear compositions and superfluid phase structures may be drastically converted [57, 61–71], which should be thoroughly investigated based on microscopic theories.

In our previous studies, under the title of “superfluid band theory,” we have pursued an approach in which superfluidity and band-structure effects are incorporated on the same footing into the density functional theory (DFT) [72–75] for the superfluid systems [28]. There has been a wealth of literature where the DFT calculations successfully elucidated structures and properties of the inner

crust matter, including pasta phases [76–84]. For the superfluid extension of the nuclear DFT, we employ a local treatment of pairing interactions, known as superfluid local density approximation (SLDA) [85–87]. By extending the framework into systems at finite temperatures and under finite magnetic-field, we have further advanced the development of a tool to comprehensively describe the structures and properties of neutron star matter under extreme conditions, such as supernova matter and magnetars [88]. In the present study, we extend our superfluid band theory to two-dimensional nuclear matter in the rod phase, which serves as a representative geometry of nuclear pasta. Our aim is to clarify how low-dimensional crystalline structures, in combination with spin-orbit interactions and strong magnetic-fields, influence neutron superfluidity, spin polarization, and pairing phases. To disentangle the roles of band-structure effects, magnetic-fields, and pairing correlations, we adopt a stepwise approach: we firstly analyze the entrainment effect within the Hartree-Fock (HF) framework (i.e., without pairing correlations), and subsequently incorporate superfluidity to investigate the interplay between spin-polarization and spin-singlet pairing, under the effect of the spin-orbit interaction. We then extend the superfluid density functional framework to include spin-triplet pairing interactions, and systematically examine the emergence of spin-triplet superfluid components by performing calculations with and without these interactions under various magnetic-field strengths. Through this unified and self-consistent framework, this work aims to provide microscopic insights into superfluid and magnetic phenomena in neutron-star crustal matter under extreme conditions.

The article is organized as follows. In Section 2, the theoretical framework of this study is briefly explained, including the spin-triplet pairing. Section 3 indicates the computational settings used in the present work. The results of the calculations are shown and discussed in Section 4. Section 5 summarizes the work and suggests future prospects.

2 FORMALISM

In this section, we present the theoretical framework employed in this study, starting from the generic formulations of the Skyrme HF and Hartree-Fock-Bogoliubov (HFB) approaches. The formulation of the superfluid band theory has been developed in our previous work [28]. For the spin-triplet pairing terms, detailed derivations can be found in Refs. [51, 89, 90], although the notation used therein differs slightly from the present formulation. The extension to finite magnetic fields is based on the general formalisms discussed in Refs. [63, 65], and their implementation within our framework has been established in Ref. [88].

2.1 Skyrme-type energy density functional and Skyrme Kohn-Sham equations

The total energy per nucleon in the neutron star matter is, in general, written as

$$E/A = \frac{1}{A} \int d\mathbf{r} [\mathcal{E}_{\text{nucl}}(\mathbf{r}) + \mathcal{E}_{\text{elec}}(\mathbf{r})], \quad (1)$$

where the nuclear part of the energy density is the sum of kinetic, interaction, Coulomb, and (for superfluid systems) pairing contributions,

$$\mathcal{E}_{\text{nucl}}(\mathbf{r}) = \mathcal{E}_{\text{kin}}(\mathbf{r}) + \mathcal{E}_{\text{int}}(\mathbf{r}) + \mathcal{E}_{\text{Coul}}(\mathbf{r}) + \mathcal{E}_{\text{pair}}(\mathbf{r}). \quad (2)$$

The kinetic and Coulomb parts are given by

$$\mathcal{E}_{\text{kin}}(\mathbf{r}) = \sum_{q=n,p} \frac{\hbar^2}{2m_q} \tau_q(\mathbf{r}), \quad (3)$$

$$\mathcal{E}_{\text{Coul}}(\mathbf{r}) = \frac{e^2}{2} \int d\mathbf{r}' \frac{\rho_p(\mathbf{r})\rho_p(\mathbf{r}')}{|\mathbf{r} - \mathbf{r}'|} + \frac{3e^2}{4} \left(\frac{3}{\pi}\right)^{1/3} \rho_p^{4/3}(\mathbf{r}), \quad (4)$$

where the exchange term of the Coulomb energy is evaluated using the Slater approximation. For the interaction part, we adopt the Skyrme-type EDF which possesses the time-even and time-odd components, provided as

$$\begin{aligned} \mathcal{E}_{\text{int}}(\mathbf{r}) &= \mathcal{E}_{\text{even}}(\mathbf{r}) + \mathcal{E}_{\text{odd}}(\mathbf{r}), \\ \mathcal{E}_{\text{even}}(\mathbf{r}) &= \sum_{t=0,1} [C_t^\rho \rho_t^2 + C_t^\alpha \rho_t^2 \rho_0^\alpha + C_t^{\Delta\rho} \rho_t \Delta\rho_t + C_t^\tau \rho_t \tau_t + C^{\nabla J} \rho_t \nabla \cdot \mathbf{J}_t - C_t^T \sum_{\mu,\nu=x}^z (J_{t,\mu\nu})^2], \\ \mathcal{E}_{\text{odd}}(\mathbf{r}) &= \sum_{t=0,1} [C_t^s \mathbf{s}_t^2 + C_t^{s\alpha} \rho_0^\alpha \mathbf{s}_t^2 + C_t^T \mathbf{s}_t \cdot \mathbf{T}_t + C_t^{\Delta s} \mathbf{s}_t \cdot \Delta \mathbf{s}_t - C_t^\tau \mathbf{j}_t^2 + C^{\nabla J} \mathbf{s}_t \cdot (\nabla \times \mathbf{j}_t)]. \end{aligned} \quad (5)$$

The coupling constants C_t^X , where X stands for ρ , τ , etc., are expressed in terms of the Skyrme force parameters, as summarized in Ref. [91]. Since the $\mathbf{s}_t \cdot \Delta \mathbf{s}_t$ term is known to induce spin instabilities [92, 93], we set $C_t^{\Delta s} = 0$ throughout this work. The local densities ρ , τ , \mathbf{j} , \mathbf{s} , \mathbf{T} , and $J_{\mu\nu}$ denote the particle density, kinetic density, current density, spin density, spin-kinetic density, and spin-current tensor density, respectively. They are constructed from the single-particle wave

functions as

$$\rho(\mathbf{r}) = \sum_{k\sigma} |\psi_{k\sigma}(\mathbf{r})|^2, \quad (6)$$

$$\tau(\mathbf{r}) = \sum_{k\sigma} |\nabla \psi_{k\sigma}(\mathbf{r})|^2, \quad (7)$$

$$\mathbf{j}(\mathbf{r}) = \sum_{k\sigma} \text{Im}[\psi_{k\sigma}^*(\mathbf{r}) \nabla \psi_{k\sigma}(\mathbf{r})], \quad (8)$$

$$\mathbf{s}(\mathbf{r}) = \sum_{k,s,s'} \boldsymbol{\sigma}_{ss'} \psi_{ks}^*(\mathbf{r}) \psi_{ks'}(\mathbf{r}), \quad (9)$$

$$\mathbf{T}(\mathbf{r}) = \sum_{k,s,s'} \boldsymbol{\sigma}_{ss'} \nabla \psi_{ks}^*(\mathbf{r}) \cdot \nabla \psi_{ks'}(\mathbf{r}), \quad (10)$$

$$J_{\mu\nu}(\mathbf{r}) = \sum_{k,s,s'} \frac{1}{2i} [\sigma_{\nu}]_{ss'} [\psi_{ks'}^*(\mathbf{r}) (\nabla_{\mu} \psi_{ks}(\mathbf{r})) - \psi_{ks}(\mathbf{r}) (\nabla_{\mu} \psi_{ks'}(\mathbf{r}))], \quad (11)$$

where $\boldsymbol{\sigma} = (\sigma_x, \sigma_y, \sigma_z)$ denotes the Pauli matrices. The spin-current tensor can be decomposed into its scalar (trace), vector, and traceless symmetric components as

$$\begin{aligned} J_t(\mathbf{r}) &= \sum_{\mu=x,y,z} J_{t,\mu\mu}(\mathbf{r}) \\ \mathbf{J}_{t,\mu}(\mathbf{r}) &= \sum_{\nu,\lambda=x,y,z} \epsilon_{\mu\nu\lambda} J_{t,\nu\lambda}(\mathbf{r}) \\ \underline{J}_{t,\mu\nu}(\mathbf{r}) &= \frac{1}{2} J_{t,\mu\nu}(\mathbf{r}) + \frac{1}{2} J_{t,\nu\mu}(\mathbf{r}) - \frac{1}{3} J_t(\mathbf{r}) \delta_{\mu\nu}. \end{aligned} \quad (12)$$

The ground state is obtained by minimizing the energy functional under the orthonormality constraint [87, 94],

$$\delta \left(E - \sum_i \epsilon_i \langle \phi_i | \phi_i \rangle \right) = 0, \quad (13)$$

leading to the spin-dependent Kohn-Sham equation:

$$\hat{h}_q \begin{pmatrix} \psi_i^{(q)}(\mathbf{r}\uparrow) \\ \psi_i^{(q)}(\mathbf{r}\downarrow) \end{pmatrix} = \epsilon_i \begin{pmatrix} \psi_i^{(q)}(\mathbf{r}\uparrow) \\ \psi_i^{(q)}(\mathbf{r}\downarrow) \end{pmatrix}, \quad (14)$$

where $q = n, p$ denotes the nucleon species. The single-particle Hamiltonian takes the general form

$$\begin{aligned} \hat{h}(\mathbf{r}) &= -\nabla \cdot (M(\mathbf{r}) + \boldsymbol{\sigma} \cdot \boldsymbol{\Lambda}(\mathbf{r})) \nabla + U(\mathbf{r}) + \boldsymbol{\sigma} \cdot \boldsymbol{\Sigma}(\mathbf{r}) \\ &+ \frac{1}{2i} [\mathbf{W}(\mathbf{r}) \cdot (\nabla \times \boldsymbol{\sigma}) + \nabla \cdot (\boldsymbol{\sigma} \times \mathbf{W}(\mathbf{r}))] + \frac{1}{2i} [\nabla \cdot \mathbf{I}(\mathbf{r}) + \mathbf{I}(\mathbf{r}) \cdot \nabla] \\ &+ \frac{1}{2i} [\nabla \cdot (\mathbf{B} \cdot \boldsymbol{\sigma}) + (\mathbf{B} \cdot \boldsymbol{\sigma}) \cdot \nabla], \end{aligned} \quad (15)$$

where the mean-field potentials can be obtained from functional derivatives,

$$\begin{aligned}\frac{\delta E}{\delta \rho} &= U(\mathbf{r}), & \frac{\delta E}{\delta \tau} &= M(\mathbf{r}), \\ \frac{\delta E}{\delta \mathbf{j}} &= \mathbf{I}(\mathbf{r}), & \frac{\delta E}{\delta \mathbf{s}} &= \boldsymbol{\Sigma}(\mathbf{r}), \\ \frac{\delta E}{\delta \mathbf{T}} &= \boldsymbol{\Lambda}(\mathbf{r}), & \frac{\delta E}{\delta \mathbf{J}} &= \mathbf{W}(\mathbf{r}), \\ \frac{\delta E}{\delta J_{\mu\nu}} &= B_{\mu\nu}(\mathbf{r}).\end{aligned}$$

Here we have omitted the isospin index q for simplicity. These potentials are explicit functionals of the local densities, and the ground state is obtained self-consistently by iteratively solving the Kohn-Sham equations.

2.2 Band theory for inner crust matter

The central idea of band theory is encapsulated in the Bloch's theorem,

$$\psi(\mathbf{r}) = \tilde{\psi}(\mathbf{r})e^{i\mathbf{k}\mathbf{r}}, \quad \tilde{\psi}(\mathbf{r} + \mathbf{R}) = \tilde{\psi}(\mathbf{r}), \quad (16)$$

where \mathbf{k} is the Bloch wave vector and \mathbf{R} is a lattice translation vector. Substituting the Bloch form into the Kohn-Sham equation (14), we obtain

$$\hat{h}_{q,\mathbf{k}} \begin{pmatrix} \tilde{\psi}_{i\mathbf{k}}^{(q)}(\mathbf{r}\uparrow) \\ \tilde{\psi}_{i\mathbf{k}}^{(q)}(\mathbf{r}\downarrow) \end{pmatrix} = \epsilon_{i\mathbf{k}} \begin{pmatrix} \tilde{\psi}_{i\mathbf{k}}^{(q)}(\mathbf{r}\uparrow) \\ \tilde{\psi}_{i\mathbf{k}}^{(q)}(\mathbf{r}\downarrow) \end{pmatrix}, \quad (17)$$

where $\hat{h}_{q,\mathbf{k}}$ can be obtained from \hat{h}_q by replacing derivatives as

$$\nabla \rightarrow \nabla + i\mathbf{k}. \quad (18)$$

In the present study, we focus on the two-dimensional crystalline configuration corresponding to the rod (or ‘‘spaghetti’’) phase in the neutron-star inner crust. The system is assumed to be uniform along the z direction, and hence the cell-periodic functions $\tilde{\psi}_{i\mathbf{k}}(\mathbf{r})$ depend only on the transverse coordinates (x, y) . As a consequence, spatial derivatives with respect to z acting on $\tilde{\psi}_{i\mathbf{k}}$ vanish, while the longitudinal Bloch wave number k_{\parallel} associated with the z direction is retained. In this formulation, the normalization is imposed on the full Bloch wave functions $\psi_{i\mathbf{k}}(\mathbf{r})$, rather than on the cell-periodic part $\tilde{\psi}_{i\mathbf{k}}(\mathbf{r})$. Specifically, the normalization is carried out over a supercell consisting of $N_{k_x} \times N_{k_y}$ unit cells in the x and y directions, respectively. Under this convention, the normalization condition for the cell-periodic function $\tilde{\psi}_{i\mathbf{k}}$ takes the form

$$\int dx dy \tilde{\psi}_{i\mathbf{k}}(x, y) = aN_{k_x}bN_{k_y}. \quad (19)$$

where a and b denote the lattice constants along the x and y directions, respectively. In the present calculations, we restrict ourselves to a square lattice, i.e., $a = b$. With this choice of normalization,

local densities are defined as spatial averages over the supercell. Accordingly, explicit factors of $(aN_{k_x})(bN_{k_y})$ appear in the expressions for the densities, reflecting the normalization volume of the Bloch states. Derivatives acting on the Bloch wave functions are evaluated using the shifted operator (18). For example, the particle density, kinetic energy density, and current density are given by

$$\rho_q(x, y) = \sum_{i\mathbf{k}\sigma} \frac{dk_{\parallel}}{2\pi(aN_{k_x})(bN_{k_y})} \left| \tilde{\psi}_{i\mathbf{k}}^{(q)}(\mathbf{r}\sigma) \right|^2 \quad (20)$$

$$\tau_q(x, y) = \sum_{i\mathbf{k}\sigma} \frac{dk_{\parallel}}{2\pi(aN_{k_x})(bN_{k_y})} \left| \nabla' \tilde{\psi}_{i\mathbf{k}}^{(q)}(\mathbf{r}\sigma) \right|^2 \quad (21)$$

$$\mathbf{j}_q(x, y) = \sum_{i\mathbf{k}\sigma} \frac{dk_{\parallel}}{2\pi(aN_{k_x})(bN_{k_y})} \text{Im} \left[\tilde{\psi}_{i\mathbf{k}}^{(q)*}(\mathbf{r}\sigma) \nabla' \tilde{\psi}_{i\mathbf{k}}^{(q)}(\mathbf{r}\sigma) \right], \quad (22)$$

where the shifted derivative operator in the present quasi-two-dimensional setup is given by

$$\nabla' = (\nabla_x + ik_x, \nabla_y + ik_y, ik_{\parallel}). \quad (23)$$

The remaining local densities are constructed in an analogous manner.

The band-structure effects on dripped neutrons in the inner crust are quantified in terms of the macroscopic effective mass [17, 24], defined through

$$m_n n_n^f = m_{n,\mu}^* n_{n,\mu}^c, \quad (24)$$

where n_n^f and $n_{n,\mu}^c$ denote the free neutron density and the conduction neutron density, respectively. The free neutron density counts neutrons that are not bound in the nuclear mean field and is evaluated as

$$n_n^f = \frac{1}{(aN_{k_x})(bN_{k_y})} \sum_{i\mathbf{k}} \frac{dk_{\parallel}}{2\pi} \theta(\mu_n - \epsilon_{i\mathbf{k}}^{(n)}) \theta(\epsilon_{i\mathbf{k}}^{(n)} - U_n^{(\max)}), \quad (25)$$

where μ_n is the neutron chemical potential and $U_n^{(\max)}$ is the maximum value of the neutron single-particle potential within the unit cell. This definition corresponds to the number of neutrons that would be mobile in the absence of band-structure effects. The conduction neutron density is defined in terms of the mobility tensor,

$$n_{n,\mu}^c = m_n \mathcal{K}^{\mu\mu}, \quad (26)$$

where the mobility coefficient is calculated from the curvature of the energy bands,

$$\mathcal{K}^{\mu\nu} = \frac{1}{(aN_{k_x})(bN_{k_y})} \sum_{i\mathbf{k}} \frac{dk_{\parallel}}{2\pi} \frac{\partial^2 \epsilon_{i\mathbf{k}}^{(n)}}{\partial k_{\mu} \partial k_{\nu}} \theta(\mu_n - \epsilon_{i\mathbf{k}}^{(n)}). \quad (27)$$

The curvature of the band dispersion reflects the mobility of particles in the crystal, and the conduction density therefore measures the fraction of dripped neutrons that can move effectively in the

presence of band-structure effects. Although we previously proposed a time-dependent approach to extract the effective mass directly [28], we employ the above standard band-theoretical definition in the present work, because our primary interest here is the modification of single-particle band structures induced by magnetic-fields and spin-orbit coupling.

2.3 Hartree-Fock-Bogoliubov theory

In the HFB theory [95], quasiparticle creation and annihilation operators $\hat{\beta}^\dagger$ and $\hat{\beta}$ are defined through the Bogoliubov transformation of the particle operators \hat{a}^\dagger and \hat{a} as

$$\begin{pmatrix} \hat{\beta} \\ \hat{\beta}^\dagger \end{pmatrix} = \begin{pmatrix} U^\dagger & V^\dagger \\ V^\top & U^\top \end{pmatrix} \begin{pmatrix} \hat{a} \\ \hat{a}^\dagger \end{pmatrix}. \quad (28)$$

The HFB ground state $|\Phi\rangle$ is defined as the quasiparticle vacuum,

$$\hat{\beta}_\mu |\Phi\rangle = 0 \quad \text{for } \forall \mu. \quad (29)$$

The coordinate-space representation is constructed using the single-particle wave functions and field operators

$$\phi_i(\mathbf{r}\sigma) = \langle \mathbf{r}\sigma | \hat{a}_i^\dagger | 0 \rangle, \quad \hat{\psi}(\mathbf{r}\sigma) = \sum_i \phi_i(\mathbf{r}\sigma) \hat{a}_i. \quad (30)$$

Within this framework, one can define not only the normal (particle) density but also the anomalous density,

$$\begin{aligned} \rho(\mathbf{r}\sigma, \mathbf{r}'\sigma') &= \langle \Phi | \psi^\dagger(\mathbf{r}'\sigma') \psi(\mathbf{r}\sigma) | \Phi \rangle, \\ \kappa(\mathbf{r}\sigma, \mathbf{r}'\sigma') &= \langle \Phi | \psi(\mathbf{r}'\sigma') \psi(\mathbf{r}\sigma) | \Phi \rangle. \end{aligned} \quad (31)$$

These densities can be expressed in terms of the quasiparticle wave functions as

$$\rho(\mathbf{r}\sigma, \mathbf{r}'\sigma') = \sum_\mu v_\mu(\mathbf{r}'\sigma') v_\mu^*(\mathbf{r}\sigma), \quad \kappa(\mathbf{r}\sigma, \mathbf{r}'\sigma') = \sum_\mu u_\mu(\mathbf{r}'\sigma') v_\mu^*(\mathbf{r}\sigma), \quad (32)$$

with quasiparticle wave functions

$$u_\mu(\mathbf{r}\sigma) = \sum_i U_{i\mu} \phi_i(\mathbf{r}\sigma), \quad v_\mu(\mathbf{r}\sigma) = \sum_i V_{i\mu} \phi_i^*(\mathbf{r}\sigma). \quad (33)$$

Owing to the fermionic anti-commutation relations, the anomalous density satisfies the antisymmetric condition

$$\kappa(\mathbf{r}\sigma, \mathbf{r}'\sigma') = -\kappa(\mathbf{r}'\sigma', \mathbf{r}\sigma). \quad (34)$$

Within the superfluid local density approximation (SLDA), this property reduces to a purely spin-antisymmetric relation,

$$\kappa_{\sigma\sigma'}(\mathbf{r}) = -\kappa_{\sigma'\sigma}(\mathbf{r}). \quad (35)$$

which allows the local anomalous density to be written in the form

$$\kappa_{\sigma\sigma'}(\mathbf{r}) = (i\sigma_y \kappa(\mathbf{r}))_{\sigma\sigma'}. \quad (36)$$

Here, $\kappa_{\sigma\sigma'}$ denotes the anomalous density matrix in the spin space, while $\kappa(\mathbf{r})$ represents the pairing order parameter expressed as a 2×2 spin matrix. The pairing order parameter can be decomposed into spin-singlet and spin-triplet components [96, 97],

$$\kappa(\mathbf{r}) = \kappa^{(s)}(\mathbf{r}) + \boldsymbol{\sigma} \cdot \boldsymbol{\kappa}^{(t)}(\mathbf{r}), \quad (37)$$

where the superscripts (s) and (t) denote singlet and triplet contributions, respectively. These components are extracted as

$$\kappa^{(s)}(\mathbf{r}) = \frac{1}{2} \text{Tr}\{-i\sigma_y \kappa_{\sigma\sigma'}(\mathbf{r})\}, \quad \kappa_{\mu}^{(t)}(\mathbf{r}) = \frac{1}{2} \text{Tr}\{-i\sigma_y \sigma_{\mu} \kappa_{\sigma\sigma'}(\mathbf{r})\}, \quad (38)$$

where the trace is taken over spin indices. Assuming that only isovector ($T = 1$) pairing channels (nn and pp) are relevant, the allowed pairing modes are restricted to s -wave spin-singlet and p -wave spin-triplet components. The singlet anomalous density reduces to the familiar expression,

$$\kappa^{(s)}(\mathbf{r}) = \frac{1}{2} (\kappa_{\uparrow\downarrow}(\mathbf{r}) - \kappa_{\downarrow\uparrow}(\mathbf{r})) = \kappa_{\uparrow\downarrow}(\mathbf{r}). \quad (39)$$

The spin-triplet pairing is characterized by the pairing spin-current tensor [51],

$$\tilde{J}_{\mu\nu}(\mathbf{r}) = -\frac{i}{2} (\partial_{\mu} - \partial'_{\mu}) \kappa_{\nu}^{(t)}(\mathbf{r}, \mathbf{r}') \Big|_{\mathbf{r}=\mathbf{r}'}. \quad (40)$$

The pairing energy is written as

$$E_{\text{pair}}^{S=0} = \int d\mathbf{r} \sum_t g_{\text{eff},t}(\mathbf{r}) \left| \kappa_t^{(s)}(\mathbf{r}) \right|^2, \quad (41)$$

$$E_{\text{pair}}^{S=1} = \int d\mathbf{r} \sum_t \tilde{C}_t^J \left| \tilde{J}_t(\mathbf{r}) \right|^2, \quad (42)$$

where g_{eff} denotes the effective pairing strength [87]. We note that \tilde{C}_t^J is different from the coefficients included in the standard Skyrme EDF C_t^J . Using the same decomposition as in Eq. (12), the spin-triplet pairing energy can be rewritten as

$$E_{\text{pair}}^{S=1} = \sum_{M=0}^2 \int d\mathbf{r} \sum_t \tilde{C}_t^{JM} \left| \tilde{J}_t^M(\mathbf{r}) \right|^2, \quad (43)$$

where $\tilde{J}_t^{M=0}$, $\tilde{J}_t^{M=1}$, and $\tilde{J}_t^{M=2}$ correspond to the scalar, vector, and traceless symmetric components of the pairing spin-current, respectively. Although these coupling constants are constrained

as $\tilde{C}_t^J = 3\tilde{C}_t^{J0} = 2\tilde{C}_t^{J1} = \tilde{C}_t^{J2}$, we treat them as independent parameters in the present study to allow for general spin-triplet pairing interactions. The specific values of these constants used in this study will be provided in the later section. Under the spherical symmetric systems, the decomposed spin-current components \tilde{J}_t^M are connected with the order parameters of the ${}^3\text{P}_M$ pairing. However, the present rod phase does not have such symmetry and it is not clear whether these pairing spin-current components and order parameters can be exactly related. This is why we call these contributions simply rank-0, rank-1, and rank-2 components, respectively. Nevertheless, we note that it is possible that they could be approximately connected even in the non-spherical rod phases.

The HFB equations take the standard matrix form

$$\begin{pmatrix} \hat{h} - \mu & \Delta \\ -\Delta^* & \hat{h}^* + \mu \end{pmatrix} \begin{pmatrix} u_\mu(\mathbf{r}) \\ v_\mu(\mathbf{r}) \end{pmatrix} = E_\mu \begin{pmatrix} u_\mu(\mathbf{r}) \\ v_\mu(\mathbf{r}) \end{pmatrix}, \quad (44)$$

where \hat{h} and Δ are 2×2 matrices in the spin space, as well as wave functions u and v are spin vectors. The spin components of the pairing field Δ are also reduced to the spin-singlet and triplet parts, which is

$$\Delta_{\sigma\sigma'}(\mathbf{r}) = (i\sigma_y)_{\sigma\sigma'} \Delta^{(s)}(\mathbf{r}) + (i\sigma_y \boldsymbol{\sigma})_{\sigma\sigma'} \cdot \boldsymbol{\Delta}^{(t)}(\mathbf{r}), \quad (45)$$

where

$$\Delta^{(s)}(\mathbf{r}) = g_{\text{eff}}(\mathbf{r}) \kappa^{(s)}(\mathbf{r}), \quad (46)$$

$$(i\sigma_y \boldsymbol{\sigma}) \cdot \boldsymbol{\Delta}^{(t)} = -\frac{i}{2} \left[\boldsymbol{\nabla} \cdot [\tilde{\mathbf{B}} \cdot (i\sigma_y \boldsymbol{\sigma})] + [\tilde{\mathbf{B}} \cdot (i\sigma_y \boldsymbol{\sigma})] \cdot \boldsymbol{\nabla} \right], \quad (47)$$

where the pairing mean field $\tilde{\mathbf{B}}$ is a spacial tensor and obtained from the functional derivative of the spin-triplet pairing energy,

$$\tilde{\mathbf{B}}_{\mu\nu}(\mathbf{r}) = 2\tilde{C}^{J0} \tilde{J}(\mathbf{r}) \delta_{\mu\nu} + 2\tilde{C}^{J1} \sum_{\lambda} \epsilon_{\lambda\mu\nu} \tilde{\mathbf{J}}_{\lambda}(\mathbf{r}) + 2\tilde{C}^{J2} \tilde{\mathbf{J}}_{\mu\nu}(\mathbf{r}). \quad (48)$$

When the band-structure effects are taken into account, the HFB Hamiltonian turns into

$$\begin{pmatrix} \hat{h}_{\mathbf{k}} - \mu & \Delta_{\mathbf{k}} \\ -\Delta_{-\mathbf{k}}^* & \hat{h}_{-\mathbf{k}}^* + \mu \end{pmatrix} \begin{pmatrix} u_{\mu\mathbf{k}}(\mathbf{r}) \\ v_{\mu\mathbf{k}}(\mathbf{r}) \end{pmatrix} = E_{\mu\mathbf{k}} \begin{pmatrix} u_{\mu\mathbf{k}}(\mathbf{r}) \\ v_{\mu\mathbf{k}}(\mathbf{r}) \end{pmatrix}, \quad (49)$$

where the indices \mathbf{k} indicate the same derivative shift (18). It should be taken care that terms belonging to $v_{\mu\mathbf{k}}$ basis yield $-\mathbf{k}$ shift instead of \mathbf{k} .

Finally, following our previous work, we quantify the spin-triplet condensations by the integrated quantities

$$S_{J_q}^{3\text{P}_M} = R^2 \int d\mathbf{r} \left| \tilde{J}_q^M(\mathbf{r}) \right|^2, \quad (50)$$

where \tilde{J}_t^M corresponds to the ${}^3\text{P}_M$ components of the pairing spin-current. The scale factor R is fixed to unity in the present study.

2.4 Extension for finite-magnetic field systems

The HF and HFB frameworks can be extended to systems under strong magnetic field by taking into account two distinct effects: (i) the modification of the nuclear single-particle Hamiltonian, and (ii) the Landau quantization of background electrons. The detailed formalism has been presented in our previous work [88], and here we briefly summarize the essential ingredients relevant to the present study.

The single-particle Hamiltonian in the presence of a magnetic-field is written as

$$\hat{h}_{q,\sigma\sigma'} = \hat{h}_{q,\sigma\sigma'}^{(0)} + \hat{h}_{q,\sigma\sigma'}^{(B)}, \quad (51)$$

where $\hat{h}_{q,\sigma\sigma'}^{(0)}$ denotes the Hamiltonian in the absence of magnetic field, while $\hat{h}_{q,\sigma\sigma'}^{(B)}$ represents the magnetic contribution. The latter consists of orbital and spin couplings,

$$\hat{h}_{q,\sigma\sigma'}^{(B)} = -\left(\mathbf{l}\delta_{qp} + g_q \frac{\boldsymbol{\sigma}}{2}\right) \cdot \tilde{\mathbf{B}}_q. \quad (52)$$

where \mathbf{l} is the orbital angular momentum operator and $\boldsymbol{\sigma}$ denotes the Pauli matrices. The orbital term acts only on protons, while the second term describes the Zeeman coupling of the nucleon spin to the magnetic field. In the present work, we neglect the orbital coupling of protons, since our primary interest lies in magnetic effects on neutron superfluidity and pairing correlations, and the orbital contribution is expected to play a minor role. The nucleon g -factors are given as

$$g_n = -3.826, \quad g_p = +5.585. \quad (53)$$

The dimensionless magnetic field entering the Hamiltonian is defined as

$$\tilde{\mathbf{B}}_q = \frac{e\hbar}{2m_q c} \mathbf{B}. \quad (54)$$

Since we are concerned with extremely strong magnetic fields, it is customary to introduce a scaled magnetic field as

$$\mathbf{B}_\star \equiv \frac{\mathbf{B}}{B_c}, \quad (55)$$

where B_c is the critical magnetic field at which the electron cyclotron energy becomes comparable to the electron rest mass,

$$B_c = \frac{m_e^2 c^3}{eh} \simeq 4.41 \times 10^{13} \text{ G}. \quad (56)$$

In principle, the magnetic field is a three-dimensional vector. However, owing to the symmetry of the rod phase, the x and y directions are equivalent. Accordingly, we consider magnetic fields oriented either along the x direction (perpendicular to the rods) or along the z direction (parallel to the rods), in the present study.

The Landau energy levels of relativistic electrons in a magnetic-field are given by

$$e_\nu = \sqrt{c^2 p^2 + m_e^2 c^4 (1 + 2\nu |B_\star|)}, \quad (57)$$

where ν is a non-negative integer labeling the Landau level and p_z is the electron momentum parallel to the magnetic field. For a fixed electron chemical potential μ_e , the allowed Landau levels satisfy

$$\nu \leq \frac{1}{2|B_\star|} \left(\frac{\mu_e^2}{m_e^2 c^4} - 1 \right). \quad (58)$$

Within this range, the electron number density and energy density are expressed as

$$n_e = \frac{2|B_\star|}{(2\pi)^2 \lambda_e^3} \sum_\nu g_\nu x_e(\nu), \quad (59)$$

$$\mathcal{E}_e = \frac{|B_\star| m_e c^2}{(2\pi)^2 \lambda_e^3} \sum_\nu g_\nu (1 + 2\nu |B_\star|) \psi_+ \left[\frac{x_e(\nu)}{\sqrt{1 + 2\nu |B_\star|}} \right] - n_e m_e c^2, \quad (60)$$

with

$$\begin{aligned} \psi_\pm(x) &= x \sqrt{1 + x^2} \pm \ln \left(x + \sqrt{1 + x^2} \right), & \gamma_e &= \frac{\mu_e}{m_e c^2}, \\ x_e(\nu) &= \sqrt{\gamma_e^2 - 1 - 2\nu |B_\star|}, & \lambda_e &= \frac{\hbar}{m_e c}. \end{aligned} \quad (61)$$

The electron chemical potential μ_e is determined self-consistently by imposing both the β -equilibrium condition, $\mu_n = \mu_p + \mu_e$, and the charge neutrality condition,

$$\frac{1}{L_x L_y} \int dx dy n_p(\mathbf{r}) = n_e. \quad (62)$$

The degree of spin-polarization for nucleons of species q is quantified by

$$P_q = \frac{N_{q,\uparrow} - N_{q,\downarrow}}{N_{q,\uparrow} + N_{q,\downarrow}}, \quad (63)$$

where the numerator is equivalent to

$$N_{q,\uparrow} - N_{q,\downarrow} = \int d\mathbf{r} [n_{q,\uparrow}(\mathbf{r}) - n_{q,\downarrow}(\mathbf{r})] = \int d\mathbf{r} s_{z,q}(\mathbf{r}). \quad (64)$$

The spin coupling to the magnetic field introduces an additional contribution to the energy density functional,

$$\mathcal{E}_{\text{mag}}(\mathbf{r}) = \sum_{q=n,p} -\mu_B g_q \mathbf{s}_q \cdot \mathbf{B}_\star, \quad (65)$$

which explicitly shows that the magnetic-field couples to the corresponding components of the spin density.

3 COMPUTATIONAL SETTINGS

3.1 General settings

In this study, we develop a dedicated numerical code to perform superfluid band calculations for two-dimensional crystalline structures. Assuming translational invariance along the z direction, the spatial domain in the x and y directions is discretized on a uniform grid with $N_x = N_y = 24$ points and a grid spacing of $\Delta x = \Delta y = 1$ fm. Accordingly, the size of the unit cell is fixed to $L_x = L_y = 24$ fm throughout this work. In the momentum space, the plane-wave wavenumbers are discretized into one hundred points with a spacing of $\Delta k = 0.015$ fm $^{-1}$ up to a cutoff $k_{\max} = 1.5$ fm $^{-1}$. For the Bloch wave vectors, the two-dimensional Brillouin zone is discretized using a uniform mesh of $N_{k_x} = N_{k_y} = 32$ points. A square lattice configuration is assumed for the crystalline structure. Single-particle wave functions are obtained by diagonalizing the HF or HFB Hamiltonian, and the calculations are iterated self-consistently until convergence of the total energy is achieved. Spatial derivatives and the Poisson equation are evaluated using the fast Fourier transform (FFT) algorithm. For the update of densities at each iteration step, the modified Broyden method is adopted. We use the SLy4 [98, 99] parameter set for the Skyrme EDF. The baryon density is fixed at $n_B = 0.04$ fm $^{-3}$, and the β -equilibrium condition described in the previous section is imposed self-consistently at each iteration step. Regarding the coupling constants of the pairing spin-current terms, there is presently no consensus on their appropriate values. In the present study, for simplicity and to isolate qualitative effects, we adopt identical coupling constants for all tensor components, i.e., $\tilde{C}_t^{J0} = \tilde{C}_t^{J1} = \tilde{C}_t^{J2} = 60$ MeV.

3.2 Structure of study

This study addresses several closely related issues: namely, (i) the entrainment effect under strong magnetic-fields, (ii) the combined influence of spin-orbit coupling and magnetic fields on spin polarization and pairing phases, and (iii) the role of spin-triplet pairing interactions in the presence of magnetic-fields. Accordingly, different forms of the Hamiltonian are employed in different parts of the analysis. In the first place, the entrainment effect is investigated within the HF framework, using the Hamiltonian given in Eq. (14), where pairing correlations are neglected. The neutron effective mass is defined through Eqs. (24)–(27), and its dependence on the magnetic-field strength is systematically examined. In the second place, superfluid effects are included to study the response of spin-polarization and spin-singlet pairing to external magnetic-fields. In this part, two calculation settings are considered: one including the spin-orbit interaction and the other neglecting it, in order to clarify its role. In the third place, the emergence of spin-triplet superfluidity is investigated by performing calculations both with and without the spin-triplet pairing energy

density functional. For each configuration, calculations are carried out over a range of magnetic-field strengths to explore how the condensation of spin-triplet components depends on external conditions.

These calculations require substantial computational resources. For the HF calculations, CPU parallelization is implemented over the Bloch wave vectors and plane-wave momenta \mathbf{k} . In the HFB calculations, the computational cost is dominated by the diagonalization of large $4N \times 4N$ Hamiltonian matrices. To accelerate this procedure, we employ GPU parallelization using the CUDA framework for Hermitian matrix operations. To reduce the overall computational cost, a part of the calculations is first performed without explicitly including the Bloch wave vectors k_x and k_y . The impact of fully incorporating band-structure effects is examined and discussed in the later sections of this paper.

4 RESULTS and DISCUSSION

In this section, we present and discuss the numerical results, organized according to their physical implications. First, we investigate the impact of the magnetic field on the neutron effective mass within the HF framework, excluding pairing correlations. Secondly, we include superfluidity to the response of the spin-singlet pairing and spin-polarization to magnetic-fields. Finally, we analyze how spin-triplet condensations are modified by the presense of the spin-triplet pairing interactions and magnetic fields.

4.1 Entrainment effects

4.1.1 Effective mass

Table 1 summarizes the calculated conduction number density and effective mass for several magnetic field strengths. Calculations are performed for two magnetic-field orientations: along the

Table 1 Calculated free neutron density, conduction number density and neutron effective mass under several magnetic-field strengths $|\mathbf{B}_\star| = 0, 100, 1000$. For the convenience of comparison, values are scaled by the average neutron density or neutron bare mass.

	$\mathbf{B} = \mathbf{0}$	$B_x = 100$	$B_x = 1000$	$B_z = 100$	$B_z = 1000$
n_n^f/n_n	0.881	0.881	0.881	0.881	0.880
n_n^c/n_n	0.586	0.577	0.380	0.578	0.389
m_n^*/m_n	1.504	1.526	2.317	1.523	2.262

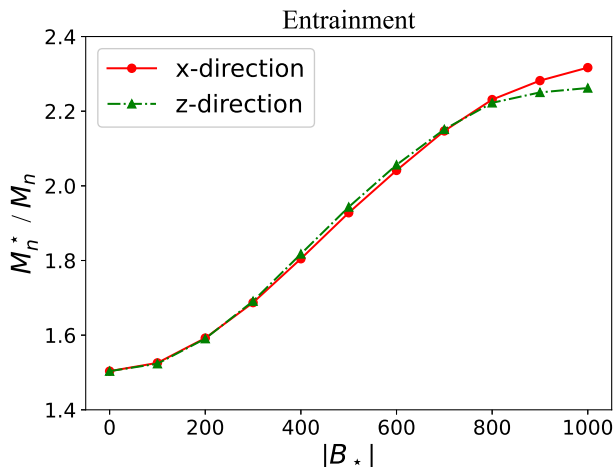


Fig. 1 Calculated neutron effective masses as a function of magnetic-field strength. The red solid (green dash-dotted) line corresponds to the results when the magnetic direction is along x -axis (z -axis) perpendicular (parallel) to the rods.

x -axis, perpendicular to the nuclear rods, and along the z -axis, parallel to the rods. The dimensionless magnetic-field strengths $B_* = 100$ and 1000 correspond to approximately 4.4×10^{15} G and 4.4×10^{16} G, respectively, both of which are within the expected range for magnetars. This table indicates that, in the absence of magnetic field, the neutron effective mass is approximately $m_n^*/m_n \simeq 1.5$, indicating a clear entrainment regime. This result is consistent with the band-theoretical calculations by Carter *et al.* [17], whereas it contrasts with previous one-dimensional studies, including Ref. [24, 27] and our earlier work [28], where anti-entrainment was observed. However, it remains unclear how these results might change when superfluidity is explicitly included or when the effective mass is derived via time-evolution calculations; thus, this point remains open for further discussion. Regarding the magnetic-field dependence, the entrainment effect remains almost unchanged for moderate field strengths around $B_* = 100$. In contrast, at $B_* = 1000$, the effective mass exceeds twice the bare neutron mass, corresponding to an enhancement by a factor of approximately 1.5 compared to the zero magnetic-field case. Figure 1 shows the effective mass as a function of magnetic-field strength, demonstrating a smooth increase from $m_n^*/m_n \simeq 1.4$ to values exceeding 2.0 over the explored range. Notably, this behavior is essentially independent of the magnetic-field orientation, with similar trends observed for both x - and z -directions. As mentioned earlier, $B_* = 100$ – 1000 corresponds to approximately 10^{15} – 10^{16} G in cgs units, a magnitude expected to exist within magnetars. These findings suggest that conventional frameworks for astrophysical dynamics, may not be applicable to magnetars in their current form.

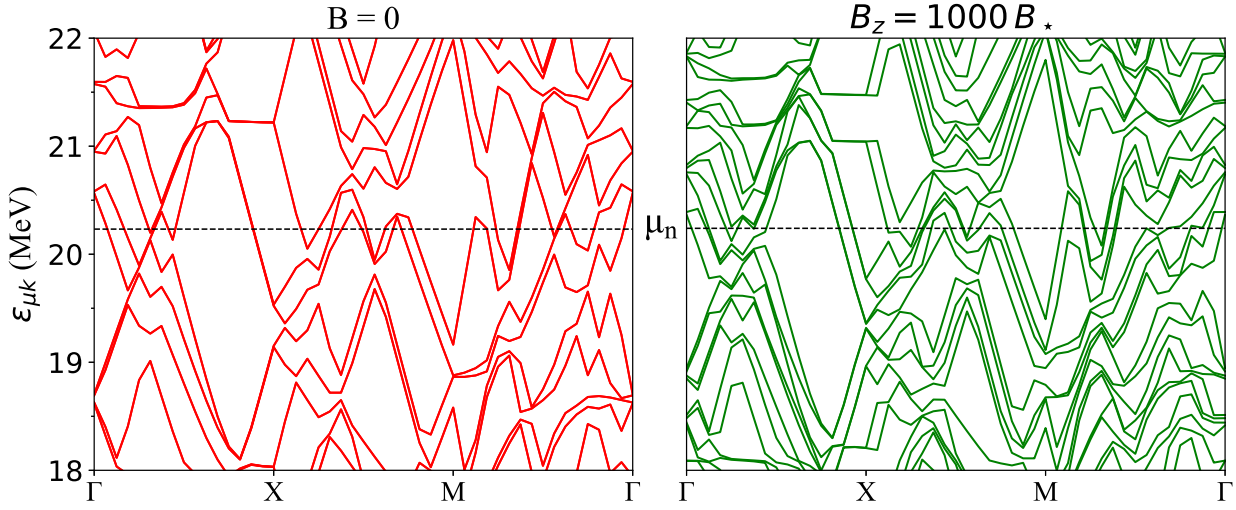


Fig. 2 The energy band diagram along a representative path in the Brillouin zone of the square lattice. The left figure shows the results of zero magnetic-field case, whereas the right is for $B_z = 1000B_*$ case. The black dashed line in two figures indicate the chemical potentials of neutrons.

Consequently, this implies the necessity for more detailed future investigations into the internal structure and dynamics of these systems in the presence of strong magnetic fields.

4.1.2 Band diagram

Figure 2 presents the calculated band structures of neutrons along a representative path in the Brillouin zone for the square lattice, both in the absence of a magnetic field (left panel) and in the presence of a magnetic field of $B_z = 1000B_*$ (right panel). In this figure, a clear enhancement of entrainment can be observed under strong magnetic fields, which can be traced back to qualitative changes in the band structure. In the zero magnetic-field case, the energy bands are doubly degenerate owing to Kramers degeneracy. When a magnetic field is applied, this degeneracy is lifted by the Zeeman effect, leading to proliferation of distinct energy bands near the Fermi surface. The resulting dense spectrum promotes band flattening through level repulsion, which in turn enhances the neutron effective mass. A simple estimate indicates that the Zeeman splitting at $B_* = 1000$ is of the order of 0.5 MeV, exceeding the typical band spacing near the Fermi level. This leads to a highly intricate band structure in that energy region and provides a microscopic explanation for the substantial increase in the effective mass. Thus, by examining the detailed band structure, we explicitly demonstrate how strong magnetic fields modify macroscopic transport properties such as the neutron effective mass.

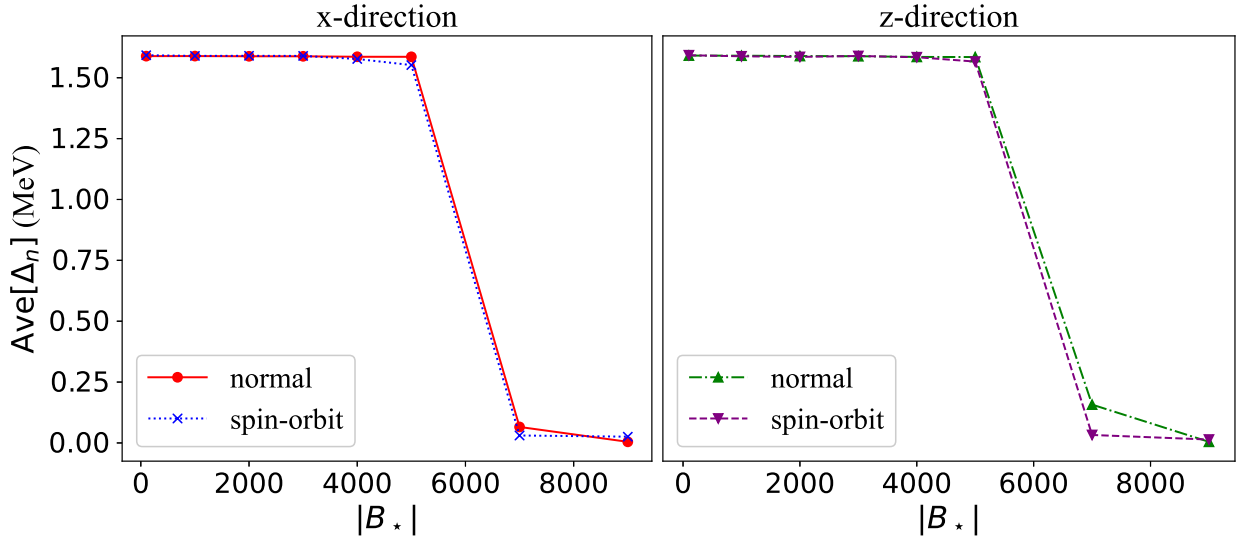


Fig. 3 The averaged pairing gaps of spin-singlet neutron superfluidity for a range of magnetic-field strengths. The left figure shows the result for the case where the magnetic-field is imposed along x -axis, while the right one is for z -axis case. In both figures, the results both when the spin-orbit EDF is present and absent is demonstrated.

4.2 Spin-orbit couplings

In this section, we present and discuss the results obtained from HFB calculations that explicitly incorporate pairing correlations. For the sake of computational simplicity, band-structure effects are neglected in this subsection by setting $N_{k_x} = N_{k_y} = 1$. The influence of band-structure effects will be examined separately in a subsequent section.

Figure 3 plots the averaged pairing gap of the spin-singlet neutron superfluid as a function of magnetic field strength. The results are displayed for magnetic fields applied along the x - and z -axes, and for cases with and without the spin-orbit term in the energy density functional. This figure indicates that the pairing gap remains nearly constant up to a certain threshold of the magnetic field strength, beyond which, it decreases abruptly and vanishes, signaling a transition to the normal phase. This qualitative behavior is robust and does not depend on the magnetic-field direction or on the inclusion of the spin-orbit interaction.

Figure 4 plots the magnitude of the neutron spin-polarization as a function of the magnetic field strength. Results for magnetic fields applied along the x - and z -axes are shown in separate panels, with calculations performed both with and without the spin-orbit term. Note that the vertical scales differ between the two panels, being of order 10^{-3} for the x -axis case and 10^{-2} for the z -axis case. Two key features can be drawn from these results. In the first place, in the absence of the spin-orbit interaction, the spin-polarization is entirely determined by the magnetic-field direction. No

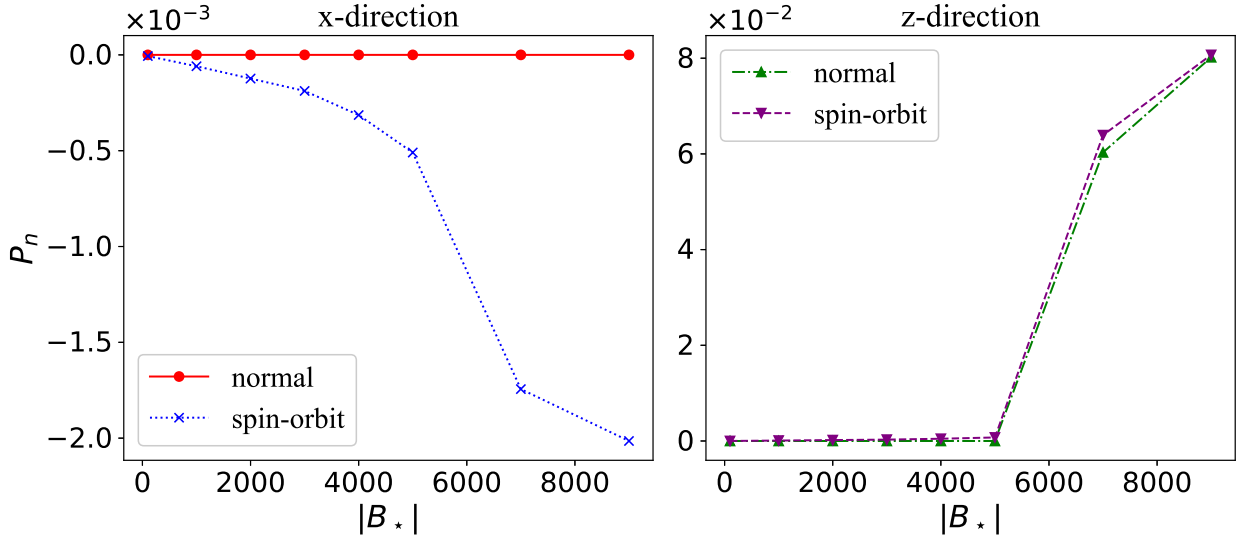


Fig. 4 The same with Fig. 3, but for the spin-polarization profiles.

polarization appears for magnetic fields applied along the x -axis, whereas for fields along the z -axis the polarization remains zero up to a threshold field strength of approximately $5000 B_*$, above which it emerges abruptly. This behavior is naturally understood from the definition of the spin-polarization in terms of the z -component of the spin density [Eq. (64)] and from the fact that the Zeeman coupling acts directly on this component. This result is also consistent with our previous findings [88]. In the second place, the inclusion of the spin-orbit interaction qualitatively modifies the polarization behaviour. Namely, a finite, albeit small, spin-polarization emerges even when the magnetic field is applied along the x -axis, with an onset at much lower field strengths of the order of $1000 B_*$. This behavior was not observed in previous one-dimensional calculations, where the spin-orbit interaction yields no contribution in the slab phase. The present results therefore demonstrate, for the first time, that the interplay between dimensionality and spin-orbit coupling can induce spin-polarization in superfluid neutron matter under magnetic fields.

4.3 Spin-triplet pairing

4.3.1 Spin-triplet EDF

In this section, we discuss the computational results concerning spin-triplet superfluid condensation. Figures 5 and 6 show the magnitude of the rank components of the neutron spin-triplet pairing as functions of the magnetic-field strengths. Figure 5 corresponds to calculations without the spin-triplet pairing EDF, while Fig. 6 presents the results obtained when this interaction is included. By comparing these two figures, three conclusions can be drawn. In the first place, in both calculations, the rank-0 component emerges abruptly once the magnetic-field strength

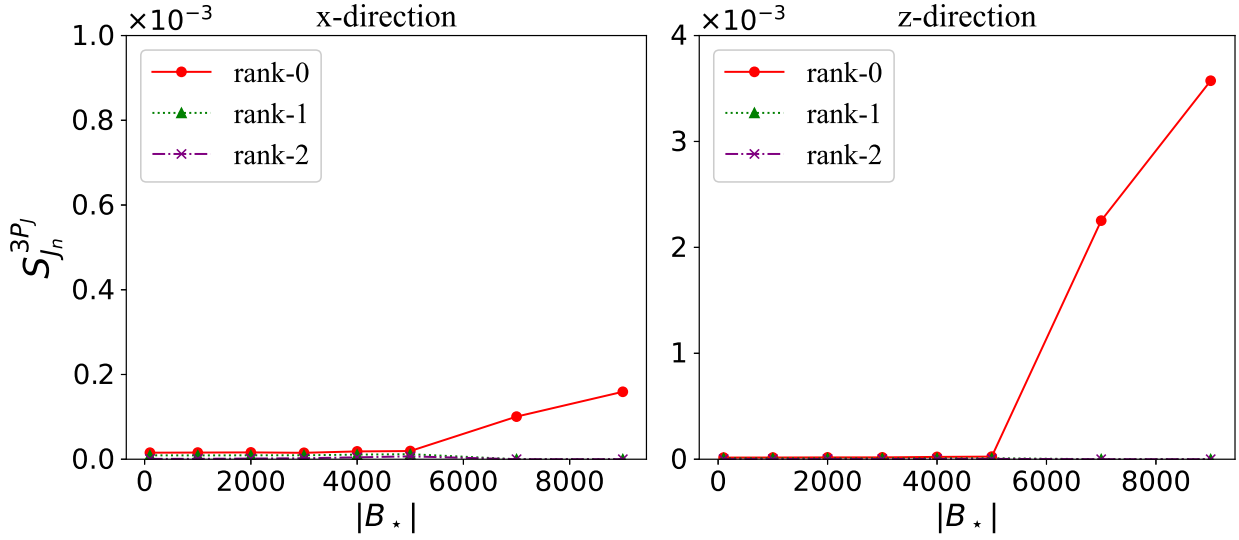


Fig. 5 The pairing condensation of each component of spin-triplet neutron superfluidity. In the left figure, the result when the magnetic-field is imposed along x -axis is shown, while the right figure is for the z -axis case. In both figures, the red solid line, green dotted line, violet dash-dotted line correspond to the sequences of rank-0, rank-1 and rank-2 components, respectively.

exceeds a critical value, reaching magnitudes of the order of 10^{-3} . This threshold takes place around $B_* = 5000$, which coincides with the critical magnetic field for the appearance of spin polarization. This correspondence indicates that the emergence of the rank-0 component is closely linked to the spin-polarized phase, consistent with previous studies highlighting the relationship between polarized neutron matter and the 3P_0 pairing order parameter [52]. In the second place, the rank-2 component never appears in the absence of the spin-triplet pairing EDF, whereas it acquires finite values whenever the corresponding interaction channel is included, largely independent of the magnetic-field strength. This result demonstrates that the 3P_2 pairing component is driven primarily by the presence of the spin-triplet interaction itself, in contrast to the 3P_0 component, which is induced by spin polarization. In the third place, the rank-1 component remains negligibly small in all cases, irrespective of the magnetic-field direction, strength, or the inclusion of the spin-triplet pairing EDF. Since the rank-1 component corresponds to the vector part of the pairing spin current, which is forbidden by spatial inversion symmetry, its suppression can be attributed to the inversion symmetry of the two-dimensional rod phase around the z -axis.

4.3.2 Band structure effects

Thus far, the results have been obtained without explicitly including Bloch wavenumbers. We now examine how band-structure effects influence spin-triplet pairing.

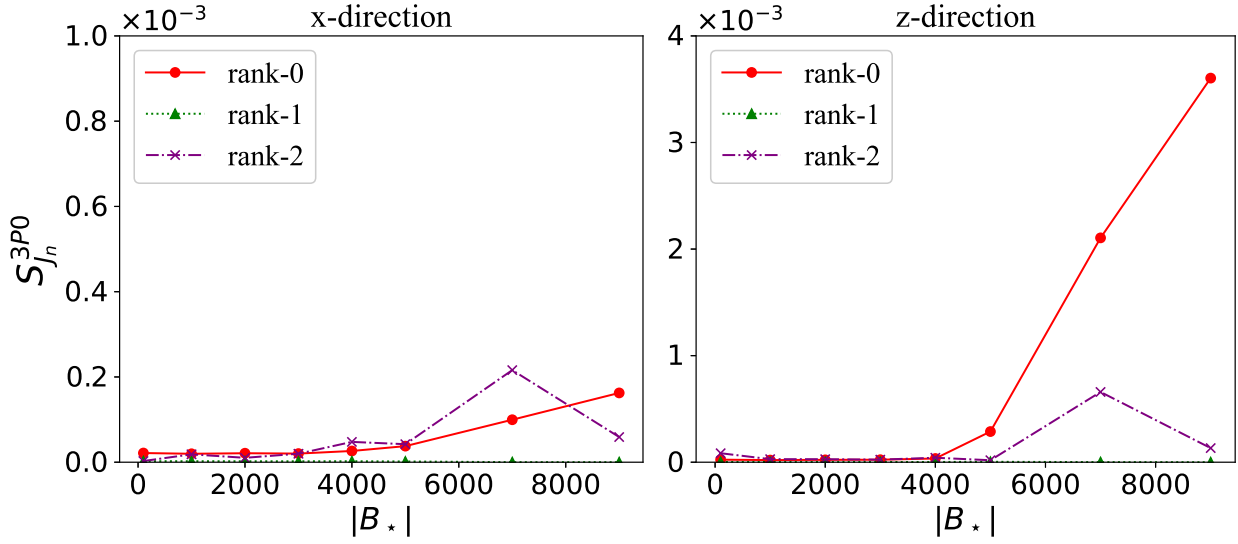


Fig. 6 The same with Fig. 5, but for the case where the spin-triplet EDF is incorporated.

Table 2 summarizes the calculated rank-0 and rank-2 components with and without band-structure effects for representative magnetic-field strengths. From this table, it is found that the qualitative dependence of each component on the magnetic-field remains essentially unchanged when band structure effects are included, although their magnitudes are quantitatively modified. An exception is found for the 3P_2 component under magnetic fields applied along the x -axis,

Table 2 The calculation results of rank-0 and rank-2 components of spin-triplet neutron superfluidity, for both cases where the band structure effects are present and absent. In all cases, results for $B_* = 1000$ and 5000 are demonstrated.

Bx			Bz		
3P0			3P0		
$ B /B_*$	No Band	Band	$ B /B_*$	No Band	Band
1000	9.13×10^{-5}	8.34×10^{-5}	1000	8.51×10^{-5}	8.53×10^{-5}
5000	1.64×10^{-4}	2.06×10^{-4}	5000	2.67×10^{-4}	2.34×10^{-4}
3P2			3P2		
$ B /B_*$	No Band	Band	$ B /B_*$	No Band	Band
1000	1.85×10^{-5}	4.38×10^{-5}	1000	6.23×10^{-6}	8.38×10^{-6}
5000	4.23×10^{-5}	2.47×10^{-4}	5000	4.17×10^{-5}	4.31×10^{-5}

where band-structure effects lead to an enhancement by approximately one order of magnitude. Nevertheless, this enhancement does not alter the overall conclusion: the emergence of spin-triplet superfluidity is governed primarily by spin-polarization and by the presence of specific interaction channels, and remains qualitatively robust against crystalline band-structure effects.

5 SUMMARY AND PROSPECTS

In this work, we have extended the framework of the superfluid band theory, developed in our previous studies, to the two-dimensional rod phase of the neutron star inner crust. Moreover, we have implemented spin-triplet pairing into the self-consistent superfluid band theory. For describing the spin-triplet neutron superfluidity, the $S = 1$ component of the anomalous density is incorporated in the superfluid DFT, on the same footing with the effects of finite magnetic-fields. Within this unified framework, we have systematically investigated spin-polarization and pairing phases by selectively switching on and off the spin-orbit interaction and spin-triplet pairing EDF.

Our main findings can be summarized as follows. In the first place, on the magnetic-fields on the order of 10^{16} G, the effective masses of neutrons increase by a factor of around 1.5 compared to no magnetized cases. This enhancement originates from a sizable modification of the band structure when the Zeeman splitting becomes comparable to the inter-level spacing. The result indicates that the conventional application of band theory to crustal matter may become questionable in magnetars, and calls for a more careful microscopic treatment of neutron dynamics under such extreme conditions. In the second place, we have examined the response of spin polarization and pairing gaps to magnetic fields, with particular attention to the role of the spin-orbit interaction. While the pairing gap has been found to depend primarily on the magnitude of the magnetic field, the spin-orbit interaction enables the emergence of weakly spin-polarized phases even for moderate field strengths and non-aligned field directions. Such effects have not been captured in previous superfluid band calculations, which were restricted to one-dimensional geometries where spin-orbit contributions vanish. Our spin-dependent HFB calculations in the two-dimensional rod phase thus reveal, for the first time, the nontrivial interplay between dimensionality, spin-orbit coupling, and magnetic fields in crustal matter. In the third place, we have systematically investigated the emergence of spin-triplet superfluid components. The results have demonstrated that the rank-0 component arises solely from magnetic-field-induced spin polarization, whereas the rank-2 component is generated by specific spin-triplet pairing interactions. By comparing calculations with and without band-structure effects, we further showed that these superfluid properties remain qualitatively robust in crystalline environments, although their magnitudes are quantitatively modified. Self-consistent nuclear calculations of neutron spin-triplet pairing remain scarce, and their application to neutron-star crust matter is pioneered in the present study. These findings provide a

microscopic basis for future investigations of astronomical simulations involving unconventional superfluid phases.

As future developments, it is highly desirable to extend the present framework to time-dependent calculations, following our previous work [28], in order to determine neutron effective masses with superfluid effects explicitly included. Although superfluid fractions in the inner crust have been investigated in several static approaches [29–32, 100], a dynamical description of superfluid motion in nuclear crystals remains largely unexplored. Another important direction is the extension to fully three-dimensional crystalline structures, where spin-triplet superfluidity and spin polarization may exhibit richer behavior. While such studies require substantial computational resources, recent advances in numerical methodologies, including the conjugate-orthogonal conjugate-gradient (COCG) [101] and related techniques [102], together with modern high-performance computing, make these extensions increasingly feasible. We hope that continued progress in microscopic nuclear theory, observational astronomy, and large-scale astrophysical simulations will ultimately lead to the comprehensive understanding of superfluid phenomena in neutron stars.

ACKNOWLEDGEMENT

We would like to appreciate Kenichi Yoshida (RCNP, Osaka University) and Nobuo Hino-hara (Tsukuba University) for the kind introduction of the formalism of the spin-triplet pairing. The author K.Y. acknowledges Shunsuke Yasunaga (Institute of Science Tokyo) who checked the formulation of this work from a theoretical point of view. This work is supported by JSPS Research Fellow, Grant No. JP24KJ1110, as well as JSPS Grant-in-Aid for Scientific Research, Grants No. JP23K03410, No. JP23K25864, and No. JP25H01269. This work mainly used the computational resources of TSUBAME4.0 at Institute of Science Tokyo, through the HPCI System Project, Project ID: hp230180, hp240183, and hp250097. Additionally this work used computational resources of the Yukawa-21 supercomputer at Yukawa Institute for Theoretical Physics (YITP), Kyoto University. This work partly used computational resource of Miyabi-C provided by Multidisciplinary Cooperative Research Program (MCRP) in Center for Computational Science, University of Tsukuba, Project ID: xg25i043. This work partly used computational resource of Fugaku provided by RIKEN through the HPCI System Research Project (Project ID: hp250288).

References

- [1] Feryal Özel and Paulo Freire, *Annu. Rev. Astron. Astrophys.*, **54**, 401–440 (2016).
- [2] J. M. Lattimer, *Annu. Rev. Nucl. Part. Sci.*, **71** (2021).
- [3] D. G. Ravenhall, C. J. Pethick, and J. R. Wilson, *Phys. Rev. Lett.*, **50**, 2066–2069 (1983).
- [4] Masa-aki Hashimoto, Hironori Seki, and Masami Yamada, *Prog Theor Phys*, **71**, 320–326 (1984).
- [5] Nicolas Chamel and Pawel Haensel, *Living Rev. Relativ.*, **11**, 10 (2008).
- [6] D. Kobyakov and C. J. Pethick, *Phys. Rev. C*, **87**, 055803 (2013).

- [7] M. E. Caplan and C. J. Horowitz, *Rev. Mod. Phys.*, **89**, 041002 (2017).
- [8] Umberto Lombardo and Hans-Josef Schulze, Superfluidity in Neutron Star Matter, In *Physics of Neutron Star Interiors*, volume 578, page 30 (2001).
- [9] D. J. Dean and M. Hjorth-Jensen, *Rev. Mod. Phys.*, **75**, 607–656 (2003).
- [10] Armen Sedrakian and John W. Clark, *Eur. Phys. J. A*, **55**, 167 (2019).
- [11] Nicolas Chamel, *Universe*, **10**, 104 (2024).
- [12] Bennett Link, Richard I. Epstein, and James M. Lattimer, *Phys. Rev. Lett.*, **83**, 3362–3365 (1999).
- [13] D. G. Yakovlev and C. J. Pethick, *Annu. Rev. Astron. Astrophys.*, **42**, 169–210 (2004).
- [14] Qiu-He Peng, Zhi-Quan Luo, and Chih-Kang Chou, *Chin. J. Astron. Astrophys.*, **6**, 297 (2006).
- [15] Peter S. Shternin, Dmitry G. Yakovlev, Craig O. Heinke, Wynn C. G. Ho, and Daniel J. Patnaude, *Mon. Not. R. Astron. Soc.*, **412**, L108–L112 (2011).
- [16] Shiqi Zhou, Erbil Gügercinoğlu, Jianping Yuan, Mingyu Ge, and Cong Yu, *Universe*, **8**, 641 (2022).
- [17] Brandon Carter, Nicolas Chamel, and Pawel Haensel, *Nuclear Physics A*, **748**, 675–697 (2005).
- [18] Nicolas Chamel, *Nuclear Physics A*, **747**, 109–128 (2005).
- [19] N. Chamel, *Phys. Rev. C*, **85**, 035801 (2012).
- [20] N. Chamel, *J Low Temp Phys*, **189**, 328–360 (2017).
- [21] N. Andersson, K. Glampedakis, W. C. G. Ho, and C. M. Espinoza, *Phys. Rev. Lett.*, **109**, 241103 (2012).
- [22] N. Chamel, *Phys. Rev. Lett.*, **110**, 011101 (2013).
- [23] Brynmor Haskell and Andrew Melatos, *Int. J. Mod. Phys. D*, **24**, 1530008 (2015).
- [24] Yu Kashiwaba and Takashi Nakatsukasa, *Phys. Rev. C*, **100**, 035804 (2019).
- [25] Gentaro Watanabe and C. J. Pethick, *Phys. Rev. Lett.*, **119**, 062701 (2017).
- [26] Yuki Minami and Gentaro Watanabe, *Phys. Rev. Res.*, **4**, 033141 (2022).
- [27] Kazuyuki Sekizawa, Sorataka Kobayashi, and Masayuki Matsuo, *Phys. Rev. C*, **105**, 045807 (2022).
- [28] Kenta Yoshimura and Kazuyuki Sekizawa, *Phys. Rev. C*, **109**, 065804 (2024).
- [29] Giorgio Almirante and Michael Urban, *Phys. Rev. C*, **109**, 045805 (2024).
- [30] Giorgio Almirante and Michael Urban, *Phys. Rev. C*, **110**, 065802 (2024).
- [31] Giorgio Almirante and Michael Urban, *Phys. Rev. Lett.*, **135**, 132701 (2025).
- [32] Giorgio Almirante, Theodora Kaskitsi, and Michael Urban, Superfluid fraction in the crystal phase of the inner crust of neutron stars (2025), arXiv:2512.18549.
- [33] H. F. Chau, K. S. Cheng, and K. Y. Ding, *Astrophys. J.*, **399**, 213 (1992).
- [34] Achim Schwenk and Bengt Friman, *Phys. Rev. Lett.*, **92**, 082501 (2004).
- [35] Dany Page, James M. Lattimer, Madappa Prakash, and Andrew W. Steiner, *Astrophys. J. Suppl. Ser.*, **155**, 623–650 (2004).
- [36] Dany Page, James M. Lattimer, Madappa Prakash, and Andrew W. Steiner, *ApJ*, **707**, 1131 (2009).
- [37] Dany Page, Madappa Prakash, James M. Lattimer, and Andrew W. Steiner, *Phys. Rev. Lett.*, **106**, 081101 (2011).
- [38] Alexander Y. Potekhin, José A. Pons, and Dany Page, *Space Sci Rev*, **191**, 239–291 (2015).
- [39] Kota Masuda and Muneto Nitta, *Phys. Rev. C*, **93**, 035804 (2016).
- [40] Kota Masuda and Muneto Nitta, *Prog Theor Exp Phys*, **2020**, 013D01 (2020).
- [41] Lev B Leinson, *Mon Not R Astron Soc*, **498**, 304–309 (2020).
- [42] Yusuke Masaki, Takeshi Mizushima, and Muneto Nitta, *Phys. Rev. Res.*, **2**, 013193 (2020).
- [43] Nils Andersson, *Universe*, **7**, 17 (2021).
- [44] Michikazu Kobayashi and Muneto Nitta, *Phys. Rev. C*, **107**, 045801 (2023).
- [45] Giacomo Marmorini, Shigehiro Yasui, and Muneto Nitta, *Sci Rep*, **14**, 7857 (2024).
- [46] J. A. Gil Granados, A. Muñoz Mateo, and X. Viñas, *Phys. Rev. C*, **111**, 065802 (2025).
- [47] Yoonhak Nam and Kazuyuki Sekizawa, Data-driven exploration of the neutron ${}^3\text{P}_2$ pairing gap using Cassiopeia A neutron star observational data (2025), arXiv:2510.20353.
- [48] Tatsuhiro Hattori and Kazuyuki Sekizawa, Exploring Interplays Between ${}^3\text{P}_2$ Neutron Superfluid Vortices and ${}^1\text{S}_0$ Proton Fluxtubes in the Outer Core of Neutron Stars (2025), arXiv:2512.22577.
- [49] Armen Sedrakian and Peter B. Rau, *Phys. Rev. D*, **111**, 023044 (2025).
- [50] Jin-Biao Wei, Fiorella Burgio, and Hans-Josef Schulze, *Universe*, **6**, 115 (2020).
- [51] Nobuo Hinohara, Tomohiro Oishi, and Kenichi Yoshida, *Phys. Rev. C*, **109**, 034302 (2024).
- [52] Hiroyuki Tajima, Hiroshi Funaki, Yuta Sekino, Nobutoshi Yasutake, and Mamoru Matsuo, *Phys. Rev. C*, **108**, L052802 (2023).
- [53] K. Makishima, T. Enoto, J. S. Hiraga, T. Nakano, K. Nakazawa, S. Sakurai, M. Sasano, and H. Murakami, *Phys. Rev. Lett.*, **112**, 171102 (2014).
- [54] R Turolla, S Zane, and A L Watts, *Rep. Prog. Phys.*, **78**, 116901 (2015).
- [55] Victoria M. Kaspi and Andrei M. Beloborodov, *Annu. Rev. Astron. Astrophys.*, **55**, 261–301 (2017).
- [56] A. Y. Potekhin and D. G. Yakovlev, Electron conduction along quantizing magnetic fields in neutron star crusts. II. Practical formulae. (1996).

- [57] A. Broderick, M. Prakash, and J. M. Lattimer, *ApJ*, **537**, 351 (2000).
- [58] A. Bonanno, L. Rezzolla, and V. Urpin, *A&A*, **410**, L33–L36 (2003).
- [59] L. Naso, L. Rezzolla, A. Bonanno, and L. Paternò, *A&A*, **479**, 167–176 (2008).
- [60] J. Frieben and L. Rezzolla, *Monthly Notices of the Royal Astronomical Society*, **427**, 3406–3426 (2012).
- [61] Paul Muzikar, J. A. Sauls, and J. W. Serene, *Phys. Rev. D*, **21**, 1494–1502 (1980).
- [62] D. Peña Arteaga, M. Grasso, E. Khan, and P. Ring, *Phys. Rev. C*, **84**, 045806 (2011).
- [63] N. Chamel, R. L. Pavlov, L. M. Mihailov, Ch. J. Velchev, Zh. K. Stoyanov, Y. D. Mutafchieva, M. D. Ivanovich, J. M. Pearson, and S. Goriely, *Phys. Rev. C*, **86**, 055804 (2012).
- [64] D. Basilico, D. Peña Arteaga, X. Roca-Maza, and G. Colò, *Phys. Rev. C*, **92**, 035802 (2015).
- [65] Martin Stein, Joachim Maruhn, Armen Sedrakian, and P.-G. Reinhard, *Phys. Rev. C*, **94**, 035802 (2016).
- [66] Martin Stein, Armen Sedrakian, Xu-Guang Huang, and John W. Clark, *Phys. Rev. C*, **93**, 015802 (2016).
- [67] Shigehiro Yasui, Chandrasekhar Chatterjee, and Muneto Nitta, *Phys. Rev. C*, **99**, 035213 (2019).
- [68] Vishal Parmar, H. C. Das, M. K. Sharma, and S. K. Patra, *Phys. Rev. D*, **107**, 043022 (2023).
- [69] Kazuyuki Sekizawa and Kentaro Kaba, Possible Existence of Extremely Neutron-Rich Superheavy Nuclei in Neutron Star Crusts Under a Superstrong Magnetic Field (2023), arXiv:2302.07923.
- [70] Wei Jiang and Yan-jun Chen, *Chinese Phys. C*, **48**, 074103 (2024).
- [71] D. Basilico, G. Colò, and Xavier Roca-Maza, *Phys. Rev. C*, **112**, 015801 (2025).
- [72] P. Hohenberg and W. Kohn, *Phys. Rev.*, **136**, B864–B871 (1964).
- [73] W. Kohn and L. J. Sham, *Phys. Rev.*, **140**, A1133–A1138 (1965).
- [74] Takashi Nakatsukasa, Kenichi Matsuyanagi, Masayuki Matsuo, and Kazuhiro Yabana, *Rev. Mod. Phys.*, **88**, 045004 (2016).
- [75] G. Colò, *Adv. Phys. X*, **5**, 1740061 (2020).
- [76] P. Magierski and P.-H. Heenen, *Phys. Rev. C*, **65**, 045804 (2002).
- [77] P. Gögelein, E. N. E. van Dalen, C. Fuchs, and H. Mütter, *Phys. Rev. C*, **77**, 025802 (2008).
- [78] W. G. Newton and J. R. Stone, *Phys. Rev. C*, **79**, 055801 (2009).
- [79] Helena Pais and Jirina R. Stone, *Phys. Rev. Lett.*, **109**, 151101 (2012).
- [80] Fabrizio Grill, Helena Pais, Constança Providência, Isaac Vidaña, and Sidney S. Avancini, *Phys. Rev. C*, **90**, 045803 (2014).
- [81] B. Schuetrumpf and W. Nazarewicz, *Phys. Rev. C*, **92**, 045806 (2015).
- [82] F. J. Fattoyev, C. J. Horowitz, and B. Schuetrumpf, *Phys. Rev. C*, **95**, 055804 (2017).
- [83] B. Schuetrumpf, G. Martínez-Pinedo, Md. Afibuzzaman, and H. M. Aktulga, *Phys. Rev. C*, **100**, 045806 (2019).
- [84] Daniel Pęczak, Agata Zdanowicz, Nicolas Chamel, Piotr Magierski, and Gabriel Wlazłowski, *Phys. Rev. X*, **14**, 041054 (2024).
- [85] Aurel Bulgac and Yongle Yu, *Phys. Rev. Lett.*, **88**, 042504 (2002).
- [86] Aurel Bulgac, *Phys. Rev. C*, **65**, 051305 (2002).
- [87] Shi Jin, Kenneth J. Roche, Ionel Stetcu, Ibrahim Abdurrahman, and Aurel Bulgac, *Computer Physics Communications*, **269**, 108130 (2021).
- [88] Kenta Yoshimura and Kazuyuki Sekizawa, *Phys. Rev. C*, **112**, 065804 (2025).
- [89] J. Dobaczewski, H. Flocard, and J. Treiner, *Nuclear Physics A*, **422**, 103–139 (1984).
- [90] T. Duguet, The Nuclear Energy Density Functional Formalism, In Christoph Scheidenberger and Marek Pfützner, editors, *The Euroscool on Exotic Beams, Vol. IV*, pages 293–350. Springer, Berlin, Heidelberg (2014).
- [91] T. Lesinski, M. Bender, K. Bennaceur, T. Duguet, and J. Meyer, *Phys. Rev. C*, **76**, 014312 (2007).
- [92] V. Hellemans, P.-H. Heenen, and M. Bender, *Phys. Rev. C*, **85**, 014326 (2012).
- [93] Kazuyuki Sekizawa and Kazuhiro Yabana, *Phys. Rev. C*, **88**, 014614 (2013).
- [94] J. A. Maruhn, P. G. Reinhard, P. D. Stevenson, and A. S. Umar, *Computer Physics Communications*, **185**, 2195–2216 (2014).
- [95] Peter Ring and Peter Schuck, *The Nuclear Many-Body Problem*, (Springer Science & Business Media, 2004).
- [96] Manfred Sigrist and Kazuo Ueda, *Rev. Mod. Phys.*, **63**, 239–311 (1991).
- [97] Manfred Sigrist, *AIP Conf. Proc.*, **789**, 165–243 (2005).
- [98] E. Chabanat, P. Bonche, P. Haensel, J. Meyer, and R. Schaeffer, *Nuclear Physics A*, **627**, 710–746 (1997).
- [99] E. Chabanat, P. Bonche, P. Haensel, J. Meyer, and R. Schaeffer, *Nuclear Physics A*, **635**, 231–256 (1998).
- [100] N. Chamel, *Phys. Rev. C*, **111**, 045803 (2025).
- [101] Shi Jin, Aurel Bulgac, Kenneth Roche, and Gabriel Wlazłowski, *Phys. Rev. C*, **95**, 044302 (2017).
- [102] Yu Kashiwaba and Takashi Nakatsukasa, *Phys. Rev. C*, **101**, 045804 (2020).